Zhou, Y., Lühr, H., Xiong, C., Pfaff, R. F. (2016): Ionospheric storm effects and equatorial plasma irregularities during the 17-18 March 2015 event. - *Journal of Geological Research*, *121*, 9, pp. 9146—9163.

DOI: http://doi.org/10.1002/2016JA023122

AGU PUBLICATIONS

JGR

Journal of Geophysical Research: Space Physics

RESEARCH ARTICLE
10.1002/2016JA023122

Special Section:
Geospace system responses to the St. Patrick's Day storms in 2013 and 2015

Ionospheric storm effects and equatorial plasma irregularities during the 17–18 March 2015 event

Yun-Liang Zhou[1,2], Hermann Lühr[2], Chao Xiong[2], and Robert F. Pfaff[3]

[1]Department of Space Physics, School of Electronic Information, Wuhan University, Wuhan, China, [2]GFZ German Research Centre for Geosciences, Potsdam, Germany, [3]NASA Goddard Space Flight Center, Heliophysics Science Division, Greenbelt, Maryland, USA

Key Points:
- Modifications of the topside ionosphere are presented for the geomagnetic storm on 17-18 March 2015
- We provide joint interpretation of storm-related plasma density variations and equatorial plasma irregularities
- Detailed discussion of the particular plasma density variations and irregularities during the recovery phase of the storm

Supporting Information:
- Supporting Information S1

Correspondence to:
H. Lühr,
hluehr@gfz-potsdam.de

Citation:
Zhou, Y.-L., H. Lühr, C. Xiong, and R. F. Pfaff (2016), Ionospheric storm effects and equatorial plasma irregularities during the 17–18 March 2015 event, *J. Geophys. Res. Space Physics*, *121*, 9146–9163, doi:10.1002/2016JA023122.

Received 1 JUL 2016
Accepted 1 SEP 2016
Accepted article online 4 SEP 2016
Published online 22 SEP 2016

Abstract The intense magnetic storm on 17–18 March 2015 caused large disturbances of the ionosphere. Based on the plasma density (*Ni*) observations performed by the Swarm fleet of satellites, the Gravity Recovery and Climate Experiment mission, and the Communications/Navigation Outage Forecasting System satellite, we characterize the storm-related perturbations at low latitudes. All these satellites sampled the ionosphere in morning and evening time sectors where large modifications occurred. Modifications of plasma density are closely related to changes of the solar wind merging electric field (E_m). We consider two mechanisms, prompt penetration electric field (PPEF) and disturbance dynamo electric field (DDEF), as the main cause for the *Ni* redistribution, but effects of meridional wind are also taken into account. At the start of the storm main phase, the PPEF is enhancing plasma density on the dayside and reducing it on the nightside. Later, DDEF takes over and causes the opposite reaction. Unexpectedly, there appears during the recovery phase a strong density enhancement in the morning/prenoon sector and a severe *Ni* reduction in the afternoon/evening sector, and we suggest a combined effect of vertical plasma drift, and meridional wind is responsible for these ionospheric storm effects. Different from earlier studies about this storm, we also investigate the influence of storm dynamics on the initiation of equatorial plasma irregularities (EPIs). Shortly after the start of the storm main phase, EPIs appear in the postsunset sector. As a response to a short-lived decline of E_m, EPI activity appears in the early morning sector. Following the second start of the main phase, EPIs are generated for a few hours in the late evening sector. However, for the rest of the storm main phase, no more EPIs are initiated for more than 12 h. Only after the onset of recovery phase does EPI activity start again in the postmidnight sector, lasting more than 7 h. This comprehensive view of ionospheric storm effects and plasma irregularities adds to our understanding of conditions that lead to ionospheric instabilities.

1. Introduction

It has long been recognized that geomagnetic storms occur in response to increased solar wind energy input. They are known to be the cause of significant ionosphere-thermosphere disturbances. The physical mechanisms responsible for ionospheric storm effects have been the topic of numerous studies during the past decades. A number of review articles [e.g., *Rishbeth and Garriott*, 1969; *Rees*, 1995; *Prölss*, 1995, 2008; *Förster and Jakowski*, 2000; *Mendillo*, 2006; *Kelley et al*., 2011] are particularly instructive for obtaining an overview.

During geomagnetic storms, in particular, during times of southward interplanetary magnetic field (IMF), large amounts of energy and momentum are deposited from the disturbed solar wind into the Earth's ionosphere-thermosphere at auroral latitudes. The most rapid reaction is the enhanced plasma convection in the high-latitude ionosphere. Fast antisunward (sunward) plasma flows over the polar cap (at auroral latitudes) drive neutral winds via ion-neutral collisions and set up a large-scale dawn-to-dusk ionospheric electric field. This high-latitude *E* field can expand almost instantaneously down to equatorial regions and is therefore termed the prompt penetration electric field (PPEF) [*Nishida*, 1968; *Kikuchi et al*., 1996; *Huang et al*., 2007]. PPEF usually causes a rapid and transient disturbance on timescales of 1–2 h [*Fejer and Emmert*, 2003; *Peymirat et al*., 2000; *Kobea et al*., 2000] and is mainly directed eastward (westward) during day (night) [*Fejer et al*., 2008]. The eastward electric field lifts up the ionosphere and causes the initial "positive ionospheric storm" at middle latitudes.

The enhanced heating of the auroral upper atmosphere will cause a sudden uplift of air and launches a so-called traveling atmospheric disturbance, which travels equatorward and drives equatorward winds

[e.g., *Richmond and Matsushita*, 1975; *Forbes et al*., 1987; *Hocke and Schlegel*, 1996; *Bruinsma and Forbes*, 2007; *Ritter et al*., 2010]. The equatorward winds, of order 150 m/s, develop due to the Coriolis effect a westward component that is growing with decreasing latitude. Meridional wind will move plasma, depending on its direction, up or down along the magnetic field lines at middle to low latitudes. This ionospheric modification is more effective on the dayside where ion/neutral collision frequencies are higher.

The storm-induced westward disturbance winds further generate a disturbance dynamo electric field (DDEF) at middle and equatorial latitudes. The resulting *E* field is directed mainly westward on the dayside and eastward on the nightside [*Blanc and Richmond*, 1980; *Huang et al*., 2005; *Yamazaki and Kosch*, 2015]. Different from the short-lived PPEF, the effects of DDEF start only 3–4 h after increase of magnetic activity, and they last longer. The DDEF typically depresses the ionosphere on the dayside initiating the "negative ionospheric storm."

Another process causing ionospheric modifications is the composition change. Storm-induced upper atmospheric upwelling transports molecular-rich air (N_2, O_2) up to F_2 region altitudes. This change in neutral composition increases significantly the recombination in the topside ionosphere [e.g., *Prölss*, 1995; *Liou et al*., 2005] and causes electron density depletions. The composition disturbance occurs primarily at high latitudes where major heating takes place. However, during magnetic storms the disturbance zone can expand to middle latitudes below 50° magnetic latitude (MLAT) and cause here a negative storm effect. In the summer hemisphere and, in particular, during early morning hours it can even expand to 30° MLAT [e.g., *Prölss*, 1993]. Conversely, neutral composition change may also cause a positive ionospheric storm, as suggested by, e.g., *Rodger et al*. [1989] or *Rishbeth* [1991]. In case of equatorward meridional winds at higher altitudes atomic oxygen-rich air can be accumulated at the equator. This will lead to an enhanced ionization rate on the dayside and consequently to an enhanced plasma density at low latitudes.

Storm-related modifications of the ionosphere have also influences on the occurrence of equatorial plasma irregularities (EPIs) on the nightside. These EPIs have attracted a lot of attention because of their negative influence on transionospheric radio signals that are commonly used for satellite communication, positioning, and timing. Good descriptions of EPI activity during magnetic storms have been given by several authors [e.g., *Basu et al*., 2010; *Pfaff et al*., 2008]. In the meantime, it is generally accepted that EPI activity in the postsunset sector is suppressed during the storm main phase [e.g., *Carter et al*., 2014, and references therein]. This is mainly caused by the enhanced westward disturbance wind during magnetic storms which suppresses the growth of the Rayleigh-Taylor (R-T) instability during postsunset hours and stabilizes the ionosphere. An exception from this rule makes the initial storm phase or impulsive intensification when the PPEF is enhancing the upward plasma drift during the prereversal enhancement (PRE) phase [e.g., *Basu et al*., 2007]. The rapid upward drift strongly favors the growth of R-T instability. Enhanced EPI activity is expected for 3–4 h in the postsunset sector.

Another storm-related effect is the generation of EPIs in the postmidnight to early morning sector [e.g., *Huang*, 2011, and references therein]. A pileup of plasma density at high altitude together with an eastward electric field at early morning hours is favoring growth of R-T instability in that sector [e.g., *Carter et al*., 2016]. The evolution of each magnetic storm is somewhat different. Therefore, only part of the effects introduced here can be expected in a single case.

In this paper, we focus on the ionospheric responses to the magnetic storm on 17–18 March 2015 (frequently termed the St. Patrick's Day storm), which is so far the largest one occurring during solar cycle 24. In a number of publications, special features of the St. Patrick's Day storm have been presented. Based on measurements from satellite missions and various ground-based networks, *Astafyeva et al*. [2015] obtained a global view of the vertical total electron content (VTEC) distribution. They reported for the main phase of the storm a hemispheric asymmetry between the American and European-African longitudinal sectors. Larger plasma density changes are observed in the Southern Hemisphere over America and in the northern over Europe. The authors attributed this to neutral composition changes. Due to the offset between geographic and magnetic poles, the composition disturbance zone reaches less far into midlatitudes over South America and Eurasia. Based on data from magnetometers, chains of ionosondes and Global Positioning System (GPS) receivers, the low-latitude ionospheric response over the Indian sector has been investigated by *Ramsingh et al*. [2015]. They attributed the suppression of the equatorial ionization anomaly (EIA) during the main phase to the disturbance wind dynamo. In another study *Tulasi Ram et al*. [2016] focused on the storm main phase

coinciding with the period of steady southward IMF B_z (12–23 UT) on 17 March 2015. Observations of the equatorial zonal electric field response are compared between dusk and premidnight sectors. It shows that the significantly enhanced zonal electric field in response to PPEF is confined to the dusk sector and lasts only a few hours. *Carter et al*. [2016] monitored the occurrence of EPI activity by means of GPS S4 scintillation receivers. They present an interpretation of their observations aided by results obtained with the Thermosphere-Ionosphere-Electrodynamic-General-Circulation-Model (TIEGCM). Although general agreement is obtained between model and observation, there are obvious differences. The model does not predict the initial EPI activity in the postsunset sector because it does not consider PPEF. More successful is the prediction of postmidnight EPIs. In this study we will make extensive use of observations presented in the papers introduced above.

The various studies of the St. Patrick's Day storm focused either on ionospheric storm effects or on the evolution of plasma irregularities. We give a comprehensive view including both these ionospheric plasma effects occurring during the storm. Our studies are primarily based on satellite data from the Gravity Recovery and Climate Experiment (GRACE), the newly launched Swarm constellation, and the Communications/Navigation Outage Forecasting System (C/NOFS) satellite. The combination of these complementary data sets provides a unique opportunity that sheds light on several storm-related questions.

In Section 2, we give a brief introduction of the data set. The ionospheric response to the storm observed by Swarm and GRACE and the dynamics of equatorial plasma irregularities during the storm are presented in section 3. In section 4 an interpretation of the observations in terms of disturbance winds and electric fields is provided, and results are discussed in the context of previous studies. Finally, we summarize our results in section 5.

2. Data Set

The Swarm mission, consisting of three spacecraft, primarily aims to measure the Earth's magnetic field and its temporal variation with unprecedented accuracy [*Friis-Christensen et al*., 2008]. On 22 November 2013 the three spacecraft were launched together into a near-polar orbit (87.5° inclination) at an initial altitude of about 490 km. After a series of orbit maneuvers the final constellation was achieved on 17 April 2014. Since then, Swarm A and C fly side-by-side at an altitude of about 470 km and with a longitudinal separation of about 1.4° (150 km), while Swarm B has a higher altitude of about 520 km at a somewhat higher inclination. This causes a slow separation of the orbital planes in local time. The payload complement of each spacecraft includes an absolute scalar magnetometer, a vector field magnetometer, an electric field instrument (EFI), an accelerometer and a set of navigation instruments. The data we primarily utilized in this study are the plasma density (*Ni*), which is measured by the Langmuir Probe (LP), part of the EFI package, at a 2 Hz sampling rate.

The Gravity Recovery and Climate Experiment (GRACE) mission, consisting of two identical spacecraft, was launched on 17 March 2002 into a near-circular, polar orbit (inclination: 89°) at an initial altitude of about 525 km [*Tapley et al*., 2004]. By March 2015 the orbit height has decreased to about 410 km. The two spacecraft follow each other at a distance of 170–220 km. Electron density data used in this study were deduced from the K-Band-Ranging system between the two GRACE spacecraft. Details on deriving the electron density from GRACE can be found in *Xiong et al*. [2010]. The obtained data set has been validated by incoherent scatter radars at European Incoherent Scatter, Millstone Hill, and Arecibo [*Xiong et al*., 2015]. Electron density estimates are available at a cadence of 5 s, but one has to keep in mind that they represent the horizontal average over about 200 km.

The Communications/Navigation Outage Forecasting System (C/NOFS) satellite was launched on 16 April 2008 into an elliptical orbit of 400 × 850 km altitude with an inclination of 13° [*de La Beaujardière et al*., 2009]. After approximately 7 years of orbital decay, the satellite altitude has lowered to 350 km at perigee and 500 km at apogee in March 2015. Since that time, C/NOFS reentered the atmosphere on 28 November 2015. Plasma density measurements are performed by three instruments: a planar Langmuir probe, a retarding potential analyzer, and a fixed-bias Langmuir probe operating in the ion mode at −3.75 V. Data from the fixed-bias Langmuir probe will be presented in this article.

During the magnetic storm on 17–18 March 2015 Swarm A and C cover the local times around 1940 LT and 0740 LT at middle and low latitudes on their upleg and downleg arcs, respectively. Swarm B cruised 1.5 h later

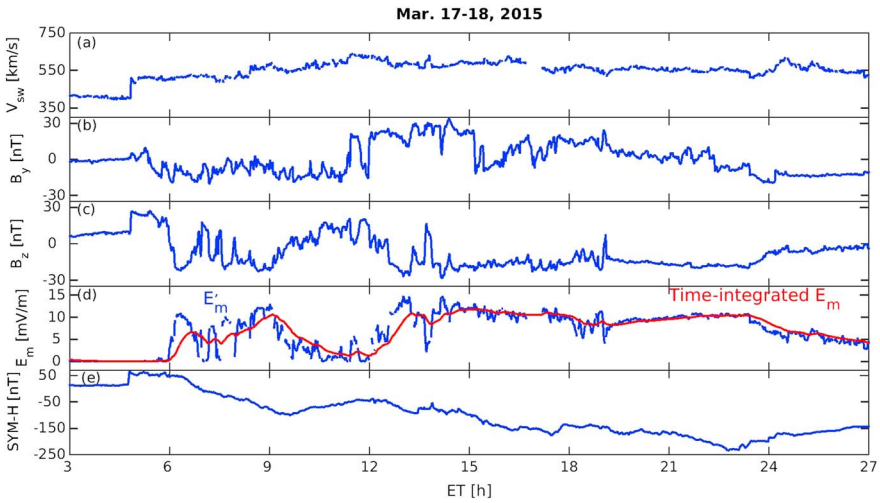

Figure 1. Solar wind and interplanetary magnetic field conditions during the St. Patrick's Day storm. In the lower panels the merging electric field, E_m, and the *SYM-H* index are shown for comparison.

in local time, around 2110 LT and 0910 LT. Similarly, the local time covered by GRACE is around 1735 LT and 0535 LT at middle and low latitudes. Along its low inclination orbit C/NOFS samples all local times every orbit. During this event Swam B is highest at about 515 km, and Swarm A/C is at about 460 km. GRACE is the lowest with an altitude of about 410 km. As Swarm A and C are separated by only about 150 km in longitude, the plasma density observations from Swarm C are almost identical with those from Swarm A. Therefore, we mainly show the observations from Swarm A.

3. Observations

In this section we present observations obtained during the magnetic storm of 17–18 March 2015 by a variety of spacecraft. Our primary aim is to study the global ionospheric response to the different phases of enhanced solar wind input. Another topic will be the occurrence of equatorial plasma irregularities during the various phases of the storm.

3.1. Solar Wind/IMF and Geomagnetic Disturbance Conditions

The severe geomagnetic storm commenced on 17 March 2015. With a minimum *SYM-H* of −234 nT it is so far the largest storm of solar cycle 24. The storm, driven by two successive southward IMF structures, is classified as a G4 (severe) level storm [*Kamide and Kusano*, 2015]. It started with a sharp increase in solar wind velocity from 420 km/s to about 500 km/s and an interplanetary magnetic field (IMF) B_z component uprise to beyond 25 nT, which was detected by the ACE satellite around 04:04 UT on 17 March 2015. As a response, a sudden storm commencement (SSC) was recorded by the *SYM-H* index with an amplitude of 67 nT at about 04:48 UT. We regard this as the moment when the coronal mass ejection swept past the Earth, and the disturbance signal reached the ground. In order to match the time of sharp increase in interplanetary parameters with the epoch of the SSC, a constant 44 min time shift (the travel time of solar wind perturbations from the L1 point to the ionosphere) was applied in this study to the solar wind and interplanetary parameters observed by ACE.

Figures 1a–1c present the temporal variation of shifted solar wind/IMF data obtained from ACE. At Figure 1e we show the *SYM-H* index evolution during 17–18 March 2015. The solar wind velocity (panel a) jumps up at the shock arrival, gradually increases during the early phase of the storm and stays around 600 km/s for the rest of the 2 days. The IMF components B_y and B_z in geocentric solar magnetospheric (GSM) coordinates are presented in Figures 1b and 1c, respectively. IMF B_z switches abruptly from positive to negative around 06:00 event time (ET) and stays negative for most of the day. A larger positive excursion is observed from 10:00 to 12:00 ET. Here the event time (ET) denotes the epoch after 17 March 2015, 00:00 UT. During the subsequent day IMF B_z fluctuates randomly about zero. IMF B_y goes negative early in the storm. At 11:20 ET it shifts to

positive values and stays predominantly positive until 22:30 ET. For the rest of the storm B_y stays negative [see also *Astafyeva et al*., 2015, Figure 1].

It is generally accepted that the merging electric field (E_m) represents a suitable coupling function between the solar wind and magnetosphere-ionosphere system. In order to interpret the ionospheric storm responses, we will relate the observed plasma density variation to the prevailing merging electric field values. We make use of the coupling function as defined by *Newell et al*. [2007]:

$$E_m^{'} = \frac{1}{3000} V_{SW}^{\frac{4}{3}} \left(\sqrt{B_y{}^2 + B_z{}^2} \right)^{\frac{2}{3}} \sin^{\frac{8}{3}}\left(\frac{\theta}{2}\right) \tag{1}$$

where V_{SW} is the solar wind velocity in km/s, B_y and B_z both in nT are the IMF components in GSM coordinates, and θ is the clock angle of the IMF. With these units the value of merging electric field will result in mV/m, comparable in size with the solar wind electric field.

It is known that variations of the interplanetary electric field (IEF) are observed almost instantaneously all over the globe due to the PPEF effect. But the transfer function between solar wind and ionospheric signal is frequency dependent. *Manoj et al*. [2008] have found that the largest ionospheric responses are obtained for signal periods of about 2 h. Furthermore, *Stolle et al*. [2008a] reported that the *F* region electron density at low latitudes responds with a delay of 1–2 h to changes of the zonal electric field. Based on these observations, we expect a delayed and smoothed response of ionospheric plasma density to changes of the IEF. This retarded reaction has been taken into account by using a similar approach as utilized in previous studies [e.g., *Richmond et al*., 2003; *Xiong et al*., 2016]:

$$E_m(t,\tau) = \frac{\int_{t1}^{t} E_m^{'}(t^{'}) e^{(t^{'}-t)/\tau} dt^{'}}{\int_{t_1}^{t} e^{(t^{'}-t)/\tau} dt^{'}} \tag{2}$$

where $E_m^{'}$ is treated as a continuous function of time t', t_1 is chosen 3 h before the actual epoch, and τ is the *e*-folding time of the weighting function in the integrands, with a value $\tau = 0.5$ h. These parameters have been found to be suitable for ionospheric studies like *Xiong et al*. [2014, and references therein]. In Figure 1d $E_m^{'}$ is presented, as calculated by equation (1), by a blue line, and the red line shows the time-integrated E_m obtained by equation (2).

For the convenience of the reader we have added the *SYM-H* index with 1 min time resolution in Figure 1e, which is commonly used for characterizing the different phases of a storm. The magnetic index stayed low at the beginning of 17 March with solar wind velocity of about 420 km/s, IMF B_y close to zero, and B_z of several nT (northward). After the increase of solar wind velocity, the *SYM-H* index showed an abrupt jump denoting the SSC of the storm. At about 06:00 ET the IMF B_z component turned sharply southward reaching a peak value of −21 nT. As a result, the *SYM-H* index started to gradually decrease, which initiated the main phase of the storm. Up to 09:37 ET the direction of IMF B_z stayed generally southward and intermitted by some short northward switches. At this time the *SYM-H* index reached a local minimum of −101 nT. After that the IMF B_z turned northward and *SYM-H* showed a slight increase. At 12:18 ET the IMF B_z component turned southward again and keep this direction for several hours until the beginning of the next day. During this period the *SYM-H* index continued to decrease and reached its minimum value of −234 nT at 22:47 ET. Thereafter, the *SYM-H* started to increase, denoting the recovery phase of this storm.

In this study we regard the evolution of the time-integrated merging electric field, E_m, as more relevant for the evolution of the plasma density. E_m sharply increased after 06:00 ET and reached a peak value of 10.6 mV/m at about 09:10 ET. As a consequence of the IMF B_z northward turning, E_m dropped suddenly to a minimum of 1.2 mV/m at about 11:30 ET. Hereafter, E_m increased again up to its maximum value of 11.9 mV/m at about 15:20 ET and stayed at a high level until the end of the day. With the beginning of the recovery phase E_m decreased to a level of 2–4 mV/m within a few hours and remained at this level for the rest of 18 March.

3.2. Ionospheric Plasma Density Response

Next, we present the ionospheric response to the different phases of the magnetic storm. Figure 2 shows the satellite observations of plasma density variations at the different geomagnetic latitudes for the storm on

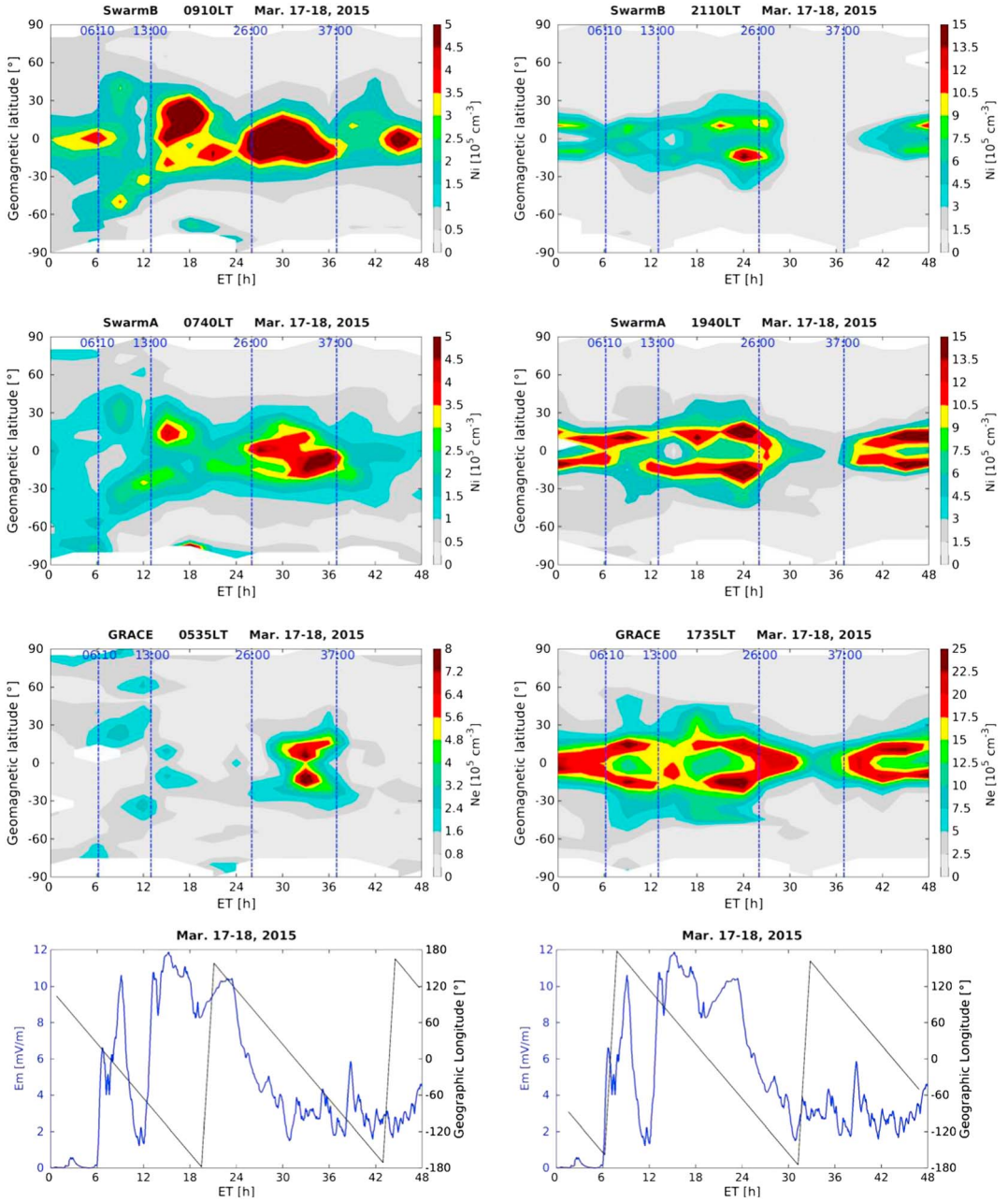

Figure 2. Plasma density variations in the ionospheric *F* region as observed by Swarm B, Swarm A, and GRACE in (left column) morning and (right column) evening sectors during the storm of 17–18 March 2015. For comparison to the storm-time effects the blue dashed vertical lines are inserted at different times in the upper three frames. (bottom row) The merging electric field (blue curve) is repeated, and the longitude of Swarm A equator crossings (black line) is shown.

17–18 March. Data from Swarm A, Swarm B, and GRACE are grouped in two columns, showing the evolution in the morning sector (left) and evening sector (right). For both local time sectors we sorted the density data into bins of magnetic latitude (MLAT) (5°) for every hour of event time. The black curve in the bottom frames reflects the longitudes at which the plasma density data have been taken. Here we used the ephemeris of Swarm A because its orbit was approximately in the middle between the two accompanying satellites. The blue curve repeats the evolution of E_m, during 17–18 March, as reference for the plasma density variations. Dashed vertical lines are inserted for better comparison of the variations within different time intervals, and the event times of the lines are listed at the top of each frame.

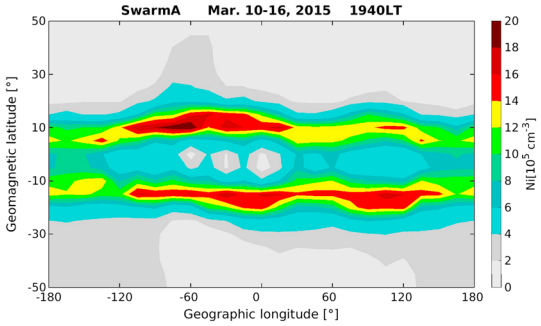

Figure 3. Global distribution of quiet-time plasma density, as an example from Swarm A observation during 10–16 March 2015 in the postsunset sector.

Before the storm onset we find typical local time distributions of the *F* region ionosphere, in the morning, low electron density before sunrise (GRACE), rather even *Ni* distribution over latitude at Swarm A (shortly after sunrise) and an early stage single peaked EIA at Swam B (0910 LT); in the evening, a well-developed EIA at Swarm A and B and a single peaked anomaly at 1735 LT (GRACE). The sharp increase of E_m around 06 ET, marking the start of storm main phase, caused in the morning sector *Ni* enhancements mainly at middle latitudes. In the evening it coincided with a weakening of the EIA and a subsequent recovery. The strong depression of E_m before 12 ET is accompanied in the morning sector by a reduction of *Ni* at all three spacecraft, but little effect is observed in the evening.

During the second and main high activity phase lasting from 13 to 26 ET, Swarm B recorded in the morning sector first a steep increase of *Ni*, in particular, in the Northern Hemisphere, which is followed some hours later by a gradual decrease. Similar density variations but with lower values are observed by Swarm A. At GRACE we find a short-lived development of an EIA during presunrise hours. Conversely on the evening side, here the EIA is first suppressed to a single peak at GRACE in the presunset sector, and it gets subsequently stronger with time. At postsunset hours (Swarm A and B) the EIA stays strong throughout this phase. Rather, interesting ionospheric features appear with the start of the recovery phase. From 26 to 37 ET we observe during morning hours a strong increase in electron density, particularly by Swarm B and somewhat less by Swarm A. GRACE finds again a well-developed EIA. This same time interval is marked in the evening by a strong depression of the equatorial ionization. At Swarm B *Ni* falls below background level, at Swarm A it gradually fades away, and at GRACE the EIA degrades to a single-peaked feature. Only 12 h after the start of the recovery phase the *F* region plasma density begins to return to preevent configurations in both local time sectors.

In fact, the satellite observations shown in Figure 2 reflect a mixture of spatial and temporal variations. Therefore, it is not easy to identify the ionospheric disturbances caused by the storm effect. In order to determine the typical quiet-time electron density background for March season and the considered local time sectors, we have taken the median of the *Ni* readings from the 7 days before the storm (10–16 March 2015). During these days the mean *Kp* was 1.7, and $Kp = 4$ occurred only once. Figure 3 shows as an example the global *Ni* distribution from Swam A in the postsunset sector. The electron density at low latitudes clearly varies with longitude. For example, a wave number 2 pattern with maxima near 60°W and 120°E can be seen. For estimating the storm-related *Ni* disturbances we have subtracted from all the satellite readings the quiet-time background values.

Figure 4 presents the ionospheric storm-time disturbances in the same format as Figure 2, at middle and low latitudes. Both enhancements and depletions of plasma density occur. Dashed vertical lines mark again the times of prominent changes. Following the storm onset at 06 ET, we find moderate density enhancements at middle latitudes in the morning sector for all three satellites. This is similar in the evening sector, except for Swarm B.

Significant changes appear right after the second E_m uprise around 13 ET. The largest response is seen in the morning sector by Swarm B recording a rapid and strong enhancement of *Ni* at low latitudes up to 30° MLAT, representing a strong ion fountain effect. Swarm A observes a similar effect but with lower amplitude. GRACE at presunrise sees just a short-lived EIA structure near the equator. All these higher densities vanish after a few hours. An inverse behavior is observed in the evening sector. It takes some hours after the E_m uprise until *Ni* anomalies appear. Highest gains are observed at low to middle latitudes and at presunset hours. Note the difference in color scale between columns. The main effect seems to be an EIA enhancement and expansion to latitudes of 30° MLAT. Prominent density anomalies appear first in the

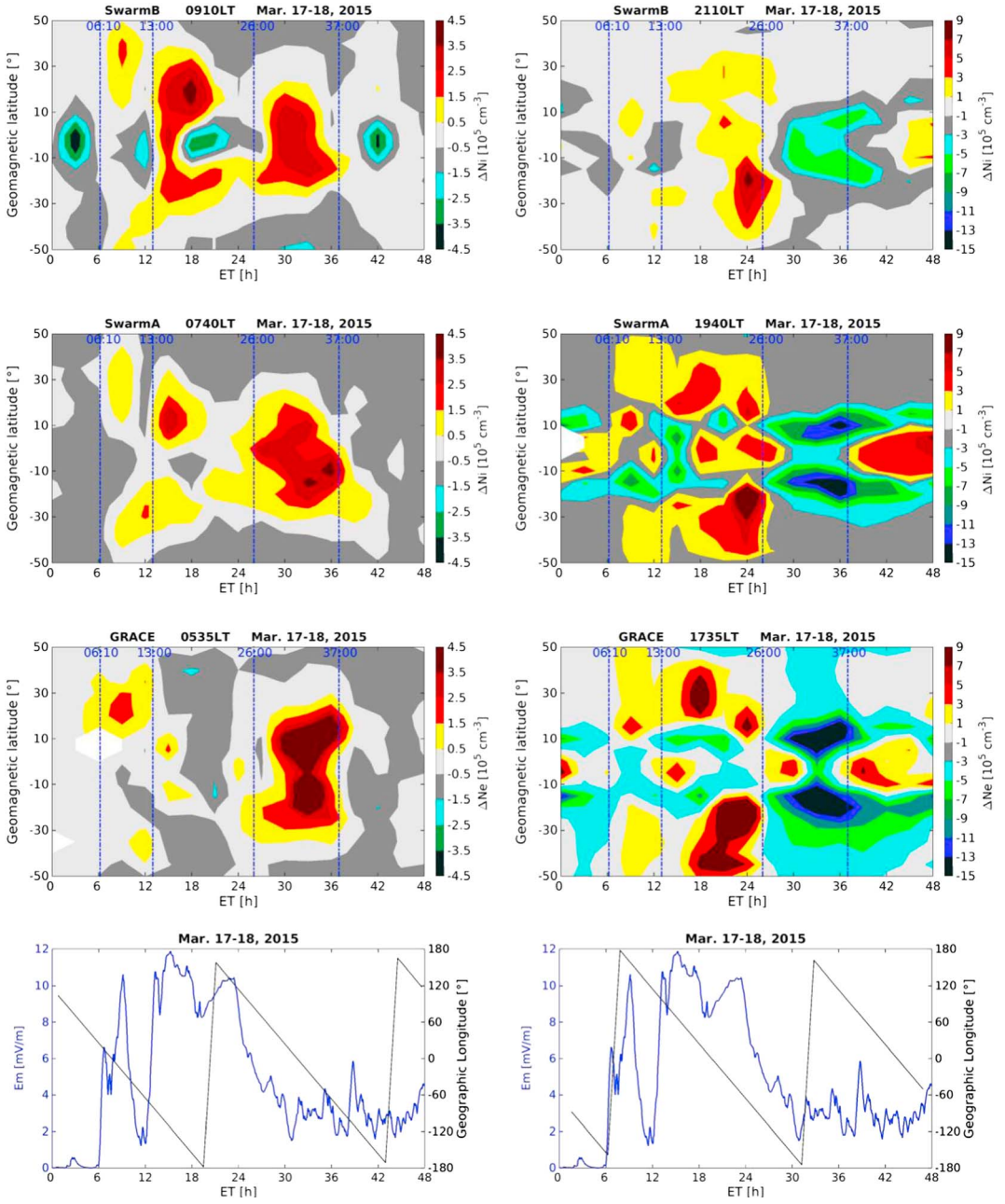

Figure 4. Same format as Figure 2 but for storm-time plasma density disturbances.

Northern Hemisphere (around 18 ET) and later even larger in the southern around 24 ET, at the end of the main phase in the late evening sector.

Shortly after the recovery phase started a major reconfiguration of the ionosphere occurs. We observe at low latitudes strong positive disturbances at all satellites in the morning sector. Largest *Ni* values are recorded during that period. A particularly strong increase of density is observed at high altitude above the equator. As evidence for that we find *Ni* values twice as large at Swarm B than at Swarm A/C (see Figure 5), although it orbits at 50 km higher altitude. Conversely in the evening sector, here a major negative disturbance of electron density occurs. At this local time sector the EIA is practically absent. This clear difference in morning/evening ionospheric response during the recovery phase is also evident in the global ΔTEC map shown in Figure 6. It took at least 12 h to restore preevent conditions. This strong and long-lasting reaction of the ionosphere during the recovery phase is quite special for this event.

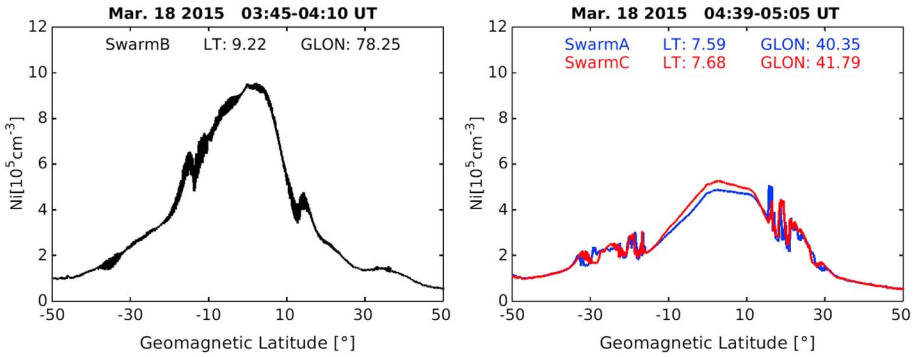

Figure 5. Major plasma density enhancement observations by Swarm at the beginning of the recovery phase. *Ni* values are almost twice as large at Swarm B although it flies about 50 km higher. (Readings of Swarm B are partly affected by instrument noise.)

3.3. Plasma Irregularities During the Storm

In the previous subsection we have referred to several intervals of E_m evolution during the course of the March 2015 storm. One would expect related changes in EPI activity during these phases. We can obtain a good global overview of EPI formation by comparing the plasma density (*Ni*) recordings of C/NOFS (flying at low inclination) with those of the polar orbiting satellites. Figure 7 shows stacked C/NOFS plots covering the interesting local time sectors, 18 to 10 LT (through midnight), for almost the entire storm period. Blue vertical lines are added for representing the local times of GRACE, Swarm A, and B at which they cross the geographic equator. Local depletions of plasma density near the equator are interpreted here as plasma bubbles or EPIs.

In Figure 7 we see that on several orbits EPIs appear in groups. The local time of their appearance changes through the course of the storm. For reference, the evolution of the merging electric field E_m is plotted in the right margin. Shortly after 06 ET there is the rapid increase of E_m, which is expected to cause an eastward PPEF and as a consequence to enhance the PRE. This strongly supports EPI formation in the postsunset region. Consistent with that notion, C/NOFS records EPI activity in the postsunset sector from about 08:30 to 10:30 ET. Swarm A/C also observes plasma bubbles around 09:30 ET and Swarm B from 08:10 to 11:30 ET on their late evening passes (see Table 1). Shortly after 09 ET E_m drops and a reversed PPEF is expected due to overshielding. As a consequence, C/NOFS detects EPI activity from 11 to 13 ET in the postmidnight sector (02 to 05 LT), whereas the EPI activity is vanishing in the postsunset sector around that time. Some postmidnight EPI activity is also observed by GRACE around 12:15 ET (see Table 1). Later, fossil bubbles cross the local times of Swarm A and B orbits.

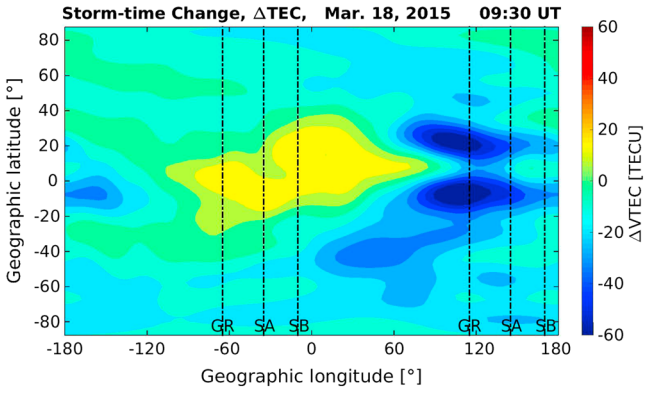

Figure 6. Global distribution of total electron content (TEC) storm-time disturbance at the end of the storm main phase. The dashed vertical lines mark the longitudes of measurements from GRACE, Swarm A, and B.

By 13 ET the storm activity has started again, as reflected by a rapidly rising E_m. An initial effect of the associated eastward PPEF is a deep depletion of *Ni* at the magnetic equator shortly before sunset, as observed around 13:25 ET by C/NOFS at 80°E to 90°E in longitude. The satellite GRACE (69°E) recorded a significant plasma density decrease already around 13 ET. We associate this depletion of the equatorial region with a strong uplift of the ionosphere (for more details see section 4.2). As a consequence, the ionosphere became unstable and favorable to EPI activity in the

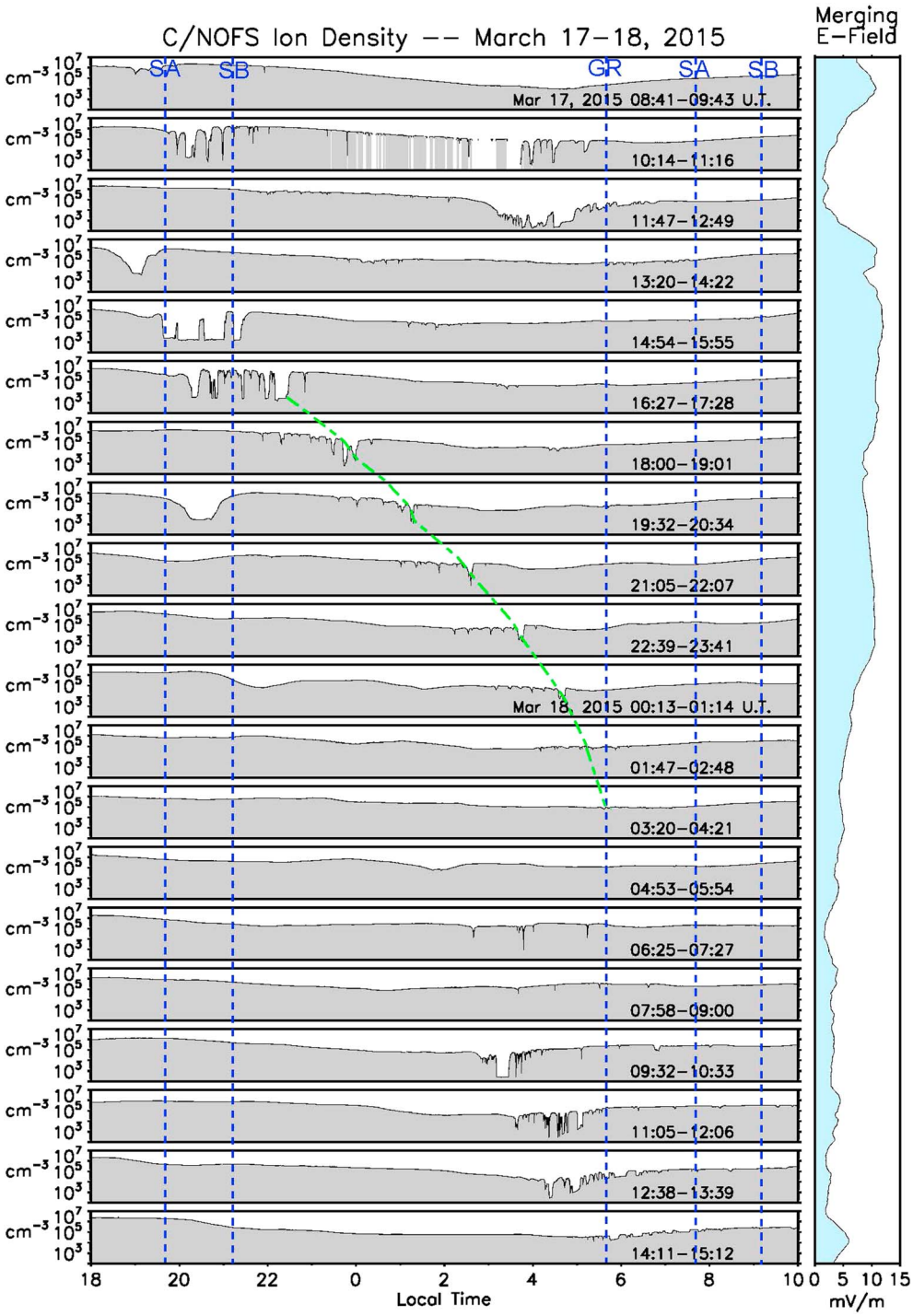

Figure 7. Equatorial plasma density variations observed by C/NOFS at low latitudes. Local depletions indicate the occurrence of equatorial plasma irregularities. The blue vertical lines are the local times when the satellites GRACE, Swarm A and B cross the equator. The green curve roughly shows the decaying and westward moving of fossil bubble structures. The evolution of the merging electric field, E_m, is shown in the right margin.

postsunset sector. This is confirmed by Swarm A/C observations around 14 ET (see Figure 8, left). Clearly visible is a wide range of plasma bubbles up to latitudes of 23° MLAT in both hemispheres and an evacuation of plasma density at low latitudes. Both facts are consistent with a strong plasma upward drift at the equator. About 2 h later Swarm B crossed this longitude region and also detected EPI activity at later local

Table 1. The Times of EPI Detections by Swarm and GRACE Spacecraft[a]

Swarm A 1940 LT	Swarm B 2110 LT	GRACE 0535 LT	Swarm A 0740 LT	Swarm B 0910 LT	Comments
	08:14				Sudden increase of E_m after 06 ET
09:24	09:50				
	11:26				Fossil EPI
		12:16			Local minimum of E_m around 12 ET
		13:47			Fossil EPI from postmidnight
			14:52	15:23	Fossil EPI
14:05					Sudden increase of E_m around 13 ET
15:39	16:10				
					No generation of EPI for 12 h
			22:37		Fossil EPI from postsunset
		24:33	24:10		Same as above
		26:04			Same as above
		27:38	27:19	27:58	Same as above
			28:52	29:33	Same as above
			30:26	31:08	Same as above
				32:43	Same as above
		32:18			Start of recovery phase effect 32 ET
		33:51	33:35		EPI activity at postmidnight
		35:24	35:11	35:54	Same as above
		36:56		37:31	Same as above
		38:28	38:18	39:07	Same as above
			39:51	40:40	Fossil EPIs from postmidnight
			41:23	42:14	Same as above

[a]Epochs are given in event time after 17 March 2015, 00:00 UT.

time (see Figure 8, right). Consistent with the Swarm observations C/NOFS observed intense EPI activity in this region during the hours from 15 to 17 ET (see Figure 7).

On later C/NOFS orbits the initiation of new irregularities has obviously ceased, and fossil bubble structures remain almost stationary in the Earth-fixed frame for more than 8 h, which is roughly marked by the green curve. This period of ceased EPI activity coincides with the main phase of the storm. But during this phase several intense substorms occurred. These can well be deduced from the auroral activity, *AE* index. Figure 9 shows the activity evolution reflected by an equivalent but local version, the *IE* index, based on data from the International Monitor for Auroral Geomagnetic Effects (IMAGE) magnetometer network [*Kauristie et al.*, 1996]. After the restart of activity around 13 UT, strong substorms occur around 18 UT and 24 UT on 17 March. Low-latitude responses that may be related to these later events are equatorial electron depletions recorded by C/NOFS around 19:40 UT and 24:30 UT (see Figure 7). But different from the plasma hole at 13:20 UT, no generation of EPIs is observed in connection with these later depletions. We will revisit this topic in section 3.2.

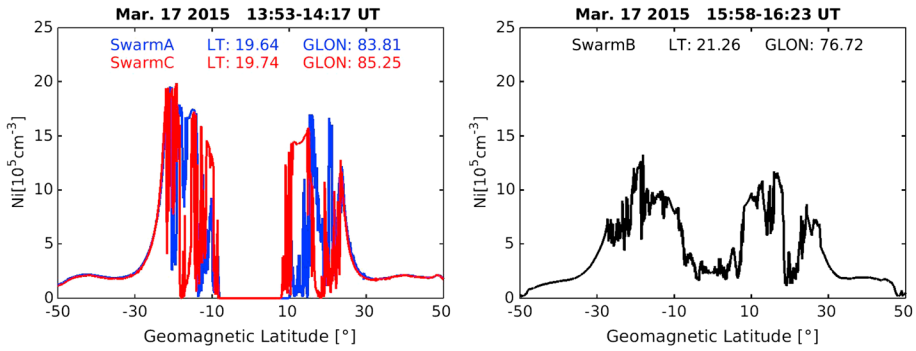

Figure 8. Strong equatorial plasma irregularity activity after the sudden increase of merging electric field around 13 UT. The equatorial ionosphere is largely evacuated.

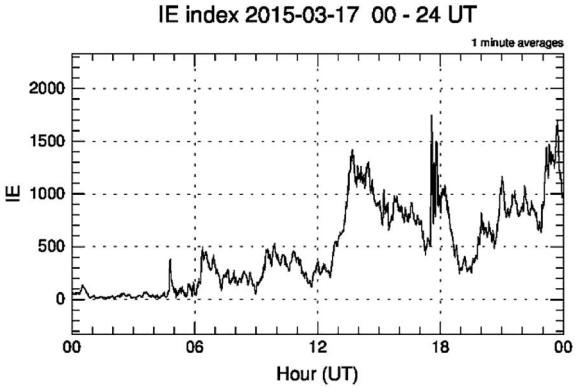

Figure 9. Temporal evolution of the auroral activity index. The *IE* index is derived from the IMAGE magnetometer data.

A new phase of EPI activity starts in the early morning sector (03 to 06 LT) around 06 UT on 18 March (see C/NOFS recordings in Figure 7), a few hours after beginning of the recovery phase. At this time the merging electric field, E_m, has already significantly decreased. It is a quite common feature that the low-latitude ionosphere in the postmidnight sector becomes unstable during the recovery phase of a storm (for more details see section 4.2). The interval of early morning EPI generation continued until about 13 UT on 18 March (see Figure 7). Thereafter, only fossil bubble features are observed moving into the dayside sector. Plasma irregularities on the dayside, associated with enhanced magnetic activity, have been reported by several researchers [e.g.,*Fukao et al*., 2003, and references therein]. *Huang et al*. [2013] suggested that dayside plasma bubbles are remnants of postmidnight EPIs.

An interesting observation to be stressed here is the lack of new EPI generation over the course of the storm main phase for at least 12 h. During that time fossil plasma bubbles rotate with the Earth into the morning sector. For better illustrating that fact, *Ni* undulations recorded by C/NOFS on successive orbits have been plotted below each other (see Figure 10). Selected time intervals have been stacked such that similar bubble features line up well. In the top panel, the segment centered at 16:40 ET, the last passage through an active irregularity region is shown. On all the subsequent orbits plasma density variations are much smoother. From the longitude changes between panels one can deduce that the bubble structures are moving westward. That is an indication for a westward disturbance wind during the storm main phase. Obtained speeds are increasing from orbit to orbit, surpassing 100 m/s after local midnight. The *Ni* undulations are extending over a range of about 30° in longitude. This range gets shorter from orbit to orbit, which is consistent with the notion that bubbles at later local time move faster westward than those at earlier local time. All these observations show that fossil plasma bubbles can be a useful tracer for ionospheric dynamics.

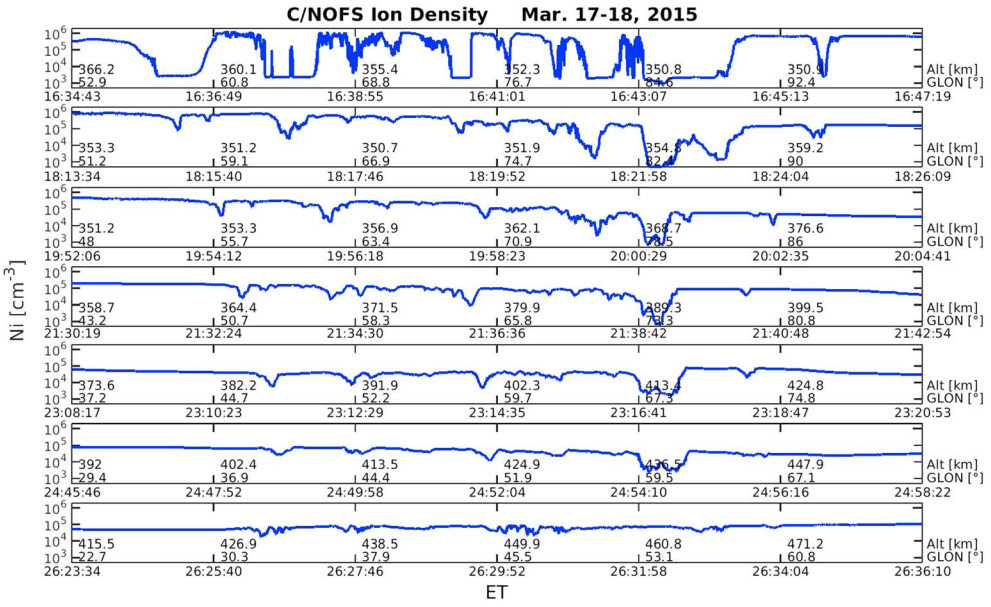

Figure 10. Persistent plasma bubble features observed by C/NOFS on successive orbits during the storm main phase. The numbers in each panel indicate the altitude and longitude of the C/NOFS position.

For completeness all individual plots of plasma density, recorded by the spacecraft Swarm, GRACE, and C/NOFS during 17 and 18 March 2015, are added as supporting information.

4. Discussion

In the previous section we have presented our observations of plasma density variations in the topside ionosphere in response to the different phases of the storm on 17–18 March 2015. Here we will try to interpret the observations in terms of disturbance electric fields and winds and discuss our findings in comparison with previous studies.

4.1. Storm-Time Disturbance of the Ionosphere

According to *Fejer et al*. [2008], the low-latitude ionosphere shows large disturbances from its quiet-time status during and after periods of enhanced geomagnetic activity. These disturbances are partly the consequence of the combined effects of prompt penetration electric fields and ionospheric disturbance dynamo. Other effects such as meridional winds and composition change may also play an important role (see *Prölss* [1995] for a review). The timescale of PPEF is typically 1–2 h, and it generally occurs in response to large and rapid changes of the magnetospheric convection pattern [*Fejer and Emmert*, 2003]. At about 06 UT on 17 March the merging electric field E_m exhibits a sudden increase to a local maximum of 6.2 mV/m and later to 10.3 mV/m. With a short time delay clear storm-related disturbances are detected by all three satellites at low to midlatitudes in the morning sector, as shown in Figure 4. It is reported by *Fejer et al*. [2008] that the prompt penetration vertical plasma drift at equinox seasons is directed upward during the hours 08 to 24 LT and downward during the rest of the day. From a statistical study, based on Republic of China Satellite - Flight 1 (ROCSAT-1) plasma drifts measurements, *Xiong et al*. [2016] deduced that the PPEF in response to a sudden increase of merging electric field is directed eastward within the local time sector 07–21 LT. According to *Prölss* [1995], plasma transport caused by eastward electric field can be identified because it moves equatorial particles up and then diffuses them poleward. Such a poleward transport is confirmed by our observations taken between 06 and 12 ET. As evident from Figure 4, plasma density enhancements appear primarily at low to midlatitudes within the 07–20 LT sector. This infers that PPEF was the main driver for plasma redistribution during the early phase of the storm.

A rather similar positive storm effect at low to midlatitudes is observed following the second enhancement of activity at 13 ET. But after a few hours, the PPEF effect has ceased, and the disturbance dynamo takes over. Evidence for that is provided by equatorward and westward winds observed after 15 ET in the midnight sector [see *Tulasi Ram et al*., 2016, Figure 5]. Consistent with the action of DDEF, we observe a negative storm effect in the morning/prenoon sector (see Figure 4). More complicated positive storm effects appear in the late evening, premidnight sector. Here obviously, a combination of an eastward directed DDEF and repeated PPEF effects due to substorms have caused the enhancement of *Ni*. Interestingly, a prominent positive disturbance appears first in the Northern Hemisphere at midlatitudes around 18 ET (see Figure 4, right column). Later, around 24 ET, a plasma enhancement in the Southern Hemisphere dominates. At both these times intense substorms occurred (see Figure 9). *Astafyeva et al*. [2015] have interpreted this as a hemispheric asymmetry revealing positive ionospheric storms first in Europe and then South America. Due to our successive sampling of these regions with satellites, we cannot decide whether the density enhancements are temporal or spatial features. Further VTEC data from the main phase presented by *Astafyeva et al*. [2015] are of interest for this study. They show a largely enhanced and poleward displaced EIA in the premidnight sector (see their Figure 2). In spite of this strong EIA, no plasma irregularities are excited during the main phase, as will be detailed in the next section.

A particularly special feature of this storm is the prominent positive ionospheric effect in the morning/prenoon sector and the corresponding negative effect at afternoon/evening hours during the recovery phase, lasting from 02 to 13 UT on 18 March. Following the arguments of *Prölss* [1995], meridional winds are the most probable cause for the *Ni* modifications in this case. Equatorward wind is pushing the ions up along the field lines. He also states that an eastward electric field is transporting on average equatorial plasma to higher altitudes. In a recent paper *Huang et al*. [2016] presented low-latitude ion drift and plasma data sampled by DMSP spacecraft (840 km altitude) in the postmidnight and morning sector. Significant upward ion drift appears with the start of the recovery phase in the morning sector (see their Figure 4). This is consistent with our observations of plasma enhancement in that time sector. Furthermore, equatorward winds

seem to have contributed also to the positive storm effect. There are clear indications that they caused an accumulation of atomic oxygen in the low-latitude topside ionosphere. This process can contribute to plasma density enhancement at high altitudes, as outlined by *Rodger et al*. [1989]. Support for that suggestion comes from *Huang et al*. [2016]. At DMSP altitude (840 km) the O^+ concentration goes up from typically less than 50% to about 90% during the recovery phase in the morning sector. Due to the fairly high level of auroral activity during the recovery phase on 18 March, some kind of equatorward disturbance wind must have persisted. During night and early morning disturbance and background winds blow equatorward, as outlined by *Fuller-Rowell et al*. [1994]. Over the cause of the storm time the effect of the disturbance wind has shifted progressively to later local times, as shown by *Huang et al*. [2016], from midnight to morning. We regard this as the reason of the positive storm effect during morning/prenoon and a negative effect at afternoon/evening hours.

4.2. The Dynamics of Equatorial Plasma Irregularities

The occurrence of plasma irregularities during the St. Patrick's Day storm has attracted the attention of several studies. For example, *Carter et al*. [2016] considered a large array of GPS S4 receivers monitoring the signal scintillation, and they interpreted also spread *F* signals from ionosondes. Both these signals are reliable indicators for ionospheric irregularities. *Tulasi Ram et al*. [2016] focused on the ionospheric response during the main phase of the storm. We will refer to the results published in these papers for interpreting our observation of plasma bubbles.

It has previously been shown [e.g., *Hanson et al*., 1986; *Su et al*., 2008; *Stolle et al*., 2008b; *Xiong et al*., 2012] that enhanced vertical plasma drift at the equator during postsunset hours is strongly favoring the formation of plasma irregularities (EPIs). Rapid increases of E_m are expected to cause an eastward PPEF; therefore, one would expect consistent changes in EPI activity during these phases. According to *Fejer et al*. [2008], PPEF effects intensify the PRE and thus support EPI formation. A first rapid increase of E_m occurred shortly after 06 ET (see Figure 1). Consistent with that notion, C/NOFS and Swarm recorded EPI activity in the late evening sector from about 08:00 to 11:00 ET (see Figure 7 and Table 1).

A second prominent increase in E_m occurred around 13 ET (see Figure 1). The effect of the corresponding PPEF has well been documented by *Tulasi Ram et al*. [2016]. At the Indian station TIR (78°E) the E_m impulse coincides with the PRE occurrence. As a response the ionosonde records a large uplift of the F_2 peak height to altitudes above 500 km within the hour 13–14 ET (see their Figure 3). It seems to be a rather localized effect. Only 20° in longitude to the east at Chumphon (CPN) in Malaysia (99°E) the ionospheric uplift is much smaller and comes later. As a consequence of the locally enhanced eastward electric field, a rapid upward plasma drift evacuates the topside ionosphere above the equator. This starts at a local time shortly before sunset. GRACE (70°E) observed already around 13 ET a clear depletion of plasma density at 1735 LT. About 25 min later C/NOFS crosses a region of very low density at longitudes from 80°E to 90°E. This plasma hole is still in sunlight, but the terminator moves gradually across it. This strong uplift of the ionosphere and evacuation of the equatorial region is favorable for the growth of R-T instability with the consequence of EPI activity in the postsunset sector. When Swarm A and C cross this plasma hole shortly after sunset around 14 ET, very intense plasma irregularities are observed (see Figure 8, left). Plasma bubbles reach up to ±23° MLAT. Clearly visible is the total depletion of electron density at low latitudes. Such a kind of extreme plasma depletion at low latitudes seems to be a storm effect and has been observed before, e.g., during the 10 November 2014 event (see Plate 2 of *Pfaff et al*. [2008]). The aforementioned EPI activity region, rather fixed in longitude, is traversed later by Swarm B (77°E) around 16:10 ET (21.26 LT, see Figure 8, right). At that time the latitudinal extend of bubble activity has even expanded to ±25° MLAT. Such an extent of affected fluxtubes, reaching up to apex heights of 2000 km, is not uncommon for magnetic storms and has been reported before [e.g., *Martinis et al*., 2015, and references therein]. C/NOFS passes this region of active EPI for the last time around 16:40 ET (see Figure 10).

Consistent with our observations, *Carter et al*. [2016] reported that S4 scintillation, peaking around 15 ET, was observed in connection with the second start of storm main phase (~13 ET) only at the stations TIR and CAL (Calcutta), India, and for a limited time (see their Figure 3). Thereafter, it was globally quiet. This agrees well with our interpretation of plasma density undulations recorded by C/NOFS after 17 UT on 17 March as fossil plasma bubbles (see Figure 10). According to *Carter et al*. [2014], the generation of plasma irregularities in the postsunset sector is suppressed during times of enhanced magnetic activity. Exceptions of that may be times

of enhanced PRE by the PPEF effect. They found that the reduction of EPI activity starts 3–4 h after *Kp* values go up. This is the time they claim that it takes for the disturbance dynamo to affect the low latitudes. In the recent study *Xiong et al*. [2016] have confirmed by means of a superposed epoch analysis that about 3 h after a sudden increase of solar wind input into the magnetosphere-ionosphere system (after the PPEF effect has ceased) westward winds and downward plasma drifts dominate for many hours in the postsunset sector. Both these forces stabilize the ionosphere. Observational evidence for the action of disturbance winds during the main phase of the 17 March 2015 storm comes from midlatitude measurements. FPI data recorded at Japan and Australia show clear westward and equatorward winds in the midnight sector after 15 ET [see *Tulasi Ram et al*., 2016, Figure 5].

When looking at the evolution of the auroral activity, as reflected by the *IE* index during the storm main phase from 13 ET to 24 ET, the prominent substorms around 18 ET and 24 ET are expected to cause significant PPEF effects. We interpret the equatorial plasma depletions recorded by C/NOFS as consequences of induced eastward electric fields. An indication for such an *E* field is also found in Swarm A and B plasma observations. There is clear evidence for enhanced equatorial ionization anomalies in the postsunset sector at the times of substorms (see Figure 2, right column, e.g., Swarm A). However, in spite of the enhanced vertical plasma drift driving the EIA, there is no indication of plasma irregularities. In our view the prevailing westward zonal wind is strong enough to suppress R-T instability even during these events. From the motion of fossil bubbles (see Figure 10) we have deduced wind speed of more than 100 m/s. Zonal ion drifts measured by DMSP are also found to be westward with speeds of about 100 m/s during the later main phase in the postmidnight sector [*Huang et al*., 2016].

Another phase of EPI activity starts in the early morning sector (03 to 06 LT) around 06 UT on 18 March (see C/NOFS recordings in Figure 7), a few hours after the beginning of the recovery phase. Also, *Carter et al*. [2016] reported the onset of scintillation signal around 06 UT on 18 March in the postmidnight sector at the African west coast and South American east coast stations (see their Figure 3). Later the activity moved gradually westward to Huancayo. S4 signal terminated around 12 UT on 18 March. All this is consistent with our EPI observations by C/NOFS, which are well complemented by latitudinal profiles of GRACE and Swarm (see Table 1).

In the postmidnight sector the conditions for a growth of the R-T instability are different from that at postsunset. According to the formalism of *Sultan* [1996] (see their equation (26)), the R-T linear growth rate depends primarily on three terms: the upward plasma drift speed, v_p, the meridional wind component normal to the L shell, u_L, and sedimentation speed, g/ν_{in}, where g is the gravitational acceleration and ν_{in} the ion-neutral collision frequency. These three terms are scaled by the vertical gradient of plasma density. *Carter et al*. [2016] deduced from experiments with the TIEGCM model that for the formation of EPI in the postmidnight sector a steep positive plasma density gradient at great height is important. In the postsunset sector the faster recombination at *E* region than at *F* region heights support the density gradient. This mechanism does not operate at postmidnight. Here the third term (sedimentation speed) is surmounting the first term (upward drift) above a certain altitude. Where upward and downward motions meet, the steepest density gradient forms and becomes the dominating factor for a positive growth rate of the R-T instability. In their TIEGCM model runs *Carter et al*. [2016] also identified the third term to be responsible for the initiation of the instability in the postmidnight sector. Later in the process the vertical plasma drift takes over control of EPI activity (see their Figure 5). Our observations confirm a large height of the F_2 peak during the recovery phase in the morning sector of 18 March. For example, Swarm B records around 04 UT on 18 March a markedly larger plasma density than Swarm A/C, which are lower by 50 km (see Figure 5). Therefore, conditions were favorable for R-T instability. This situation of plasma pileup in the morning sector ended around 13 UT on 18 March (see Figure 4). At about the same time the postmidnight EPI activity ended (see Figure 7 for C/NOFS observations and *Carter et al*. [2016, Figure 3]). All these observations provide further evidence for the processes, as outlined by *Carter et al*. [2016], which destabilize the ionosphere in the early morning sector.

5. Summary and Conclusion

In this study we have investigated ionospheric modifications during the severe magnetospheric storm on 17–18 March 2015. Based on plasma density observations from the Swarm constellation, GRACE satellites, and from C/NOFS, a detailed picture of the storm-induced effects could be presented. It is just the fortunate

combination of low-latitude observations (C/NOFS) with polar-orbit sampling at three well-spaced local times both in the morning and evening sectors that provides a rather comprehensive view of plasma density variations. Different from other studies about this storm, we investigated the modification of *F* region plasma density and the associated occurrence of equatorial plasma irregularities side-by-side. This helps to understand the processes that are responsible for low-latitude ionospheric instabilities during magnetic storms. Major findings can be summarized as follows:

1. Important changes of plasma density occur after rapid increases of the dayside merging electric field, E_m, both in the morning/prenoon and evening/postsunset sectors. In response to the eastward prompt penetration electric field (PPEF) a positive ionospheric storm effect is observed over the local time range from 07 to 20 LT. Plasma density enhancements appear primarily at low to middle latitudes. Both these effects are observed in response to the two rapid E_m increases on 17 March.
2. A few hours after start of the main phase the effect of the disturbance dynamo electric field takes over control. As a response we observe a gradual reduction of ΔNi on the dayside but an enhancement of the plasma fountain effect in the postsunset sector.
3. A particularly interesting feature of this storm is the prominent ionospheric modification during the recovery phase. A strong positive storm effect appears in the morning/prenoon sector, and a correspondingly strong negative ionospheric effect is observed during afternoon/postsunset hours. We suggest a combined effect of vertical plasma drift and meridional winds as primary cause for these storm-related modifications. Additional studies are needed to confirm this inference.

All these three ionospheric storm features are associated with different responses of equatorial plasma irregularities (EPIs), which are detailed below:

4. Rapid increases of E_m are associated with eastward PPEF, which in turn amplify the prereversal enhancement. This favors the growth of R-T instability in the postsunset sector and causes EPI activity in a limited longitude range. We have observed periods of EPI activity after the first and second uprise of E_m on 17 March. However, EPI activity ceased after a few hours because the PPEF does not last long.
5. Enhanced magnetic activity during the storm main phase suppresses the R-T instability with a delay of about 3 h after the onset. Equatorward and westward directed winds stabilize the postsunset ionosphere after they have reached low latitudes. As a consequence we observe no new irregularities for 12 h during the storm main phase.
6. Postmidnight plasma irregularities form when steep radial plasma density gradient appear at great heights. This situation occurred on 18 March during the recovery phase. Dense plasma had piled up over the equator in the morning sector. As a consequence EPI activity could be observed for 7 h at local times 02–05 LT. After depletion of plasma density, the EPI activity ceased.

This so-called St. Patrick's Day storm has exhibited a number of interesting ionospheric features. Here we have presented only a few of them. Several others would warrant further investigations.

Acknowledgments

The European Space Agency (ESA) is acknowledged for providing the Swarm data. The electron density is obtained from http://earth.esa.int/swarm. The GRACE mission is sponsored by the Space Agency of the German Aerospace Center (DLR) through funds of the Federal Ministry of Economics and Technology. The GRACE data are available at the Information System and Data Center (ISDC) of GFZ German Research Centre for Geosciences. Data set names are as follows: GA-OG-1B-NAVSOL, GB-OG-1B-NAVSOL, and GX-OG-1B-KBRDAT. The solar wind and interplanetary magnetic field data are derived from NASA's ACE mission, and they can be found at http://www.srl.caltech.edu/ACE/ASC/level2/. The *SYM-H* data are provided by the World Data Center for Geomagnetism, Kyoto, and downloaded from http://wdc.kugi.kyoto-u.ac.jp/aeasy/index.html. The global ionospheric maps (GIM) are available from ftp://cddis.gsfc.nasa.gov/gps/products/ionex/. The work of Yun-Liang Zhou is supported by the National Nature Science Foundation of China (41274194 and 41431073) and China Scholarship Council (201506275011).

References

Astafyeva, E., I. Zakharenkova, and M. Förster (2015), Ionospheric response to the 2015 St. Patrick's Day storm: A global multi-instrumental overview, *J. Geophys. Res. Space Physics*, *120*, 9023–9037, doi:10.1002/2015JA021629.

Basu, S., S. Basu, F. J. Rich, K. M. Groves, E. MacKenzie, C. Coker, Y. Sahai, P. R. Fagundes, and F. Becker-Guedes (2007), Response of the equatorial ionosphere at dusk to penetration electric fields during intense magnetic storms, *J. Geophys. Res.*, *112*, A08308, doi:10.1029/2006JA012192.

Basu, S., S. Basu, E. MacKenzie, C. Bridgwood, C. E. Valladares, K. M. Groves, and C. Carrano (2010), Specification of the occurrence of equatorial ionospheric scintillations during the main phase of large magnetic storms within solar cycle 23, *Radio Sci.*, *45*, RS5009, doi:10.1029/2009RS004343.

Blanc, M., and A. D. Richmond (1980), The ionospheric disturbance dynamo, *J. Geophys. Res.*, *85*, 1669–1686, doi:10.1029/JA085iA04p01669.

Bruinsma, S. L., and J. M. Forbes (2007), Global observation of traveling atmospheric disturbances (TADs) in the thermosphere, *Geophys. Res. Lett.*, *34*, L14103, doi:10.1029/2007GL030243.

Carter, B. A., et al. (2014), Geomagnetic control of equatorial plasma bubble activity modeled by the TIEGCM with *Kp*, *Geophys. Res. Lett.*, *41*, 5331–5339, doi:10.1002/2014GL060953.

Carter, B. A., E. Yizengaw, R. Pradipta, J. M. Retterer, K. Groves, C. Valladares, R. Caton, C. Bridgwood, R. Norman, and K. Zhang (2016), Global equatorial plasma bubble occurrence during the 2015 St. Patrick's Day storm, *J. Geophys. Res. Space Physics*, *121*, 894–905, doi:10.1002/2015JA022194.

de La Beaujardière, O., et al. (2009), C/NOFS observations of deep plasma depletions at dawn, *Geophys. Res. Lett.*, *36*, L00C06, doi:10.1029/2009GL038884.

Fejer, B. G., and J. T. Emmert (2003), Low-latitude ionospheric disturbance electric field effects during the recovery phase of the 19–21 October 1998 magnetic storm, *J. Geophys. Res.*, *108*(A12), 1454, doi:10.1029/2003JA010190.

Fejer, B. G., J. W. Jensen, and S.-Y. Su (2008), Seasonal and longitudinal dependence of equatorial disturbance vertical plasma drifts, *Geophys. Res. Lett.*, *35*, L20106, doi:10.1029/2008GL035584.
Forbes, J. M., R. G. Roble, and F. A. Marcos (1987), Thermospheric dynamics during the March 22, 1979, magnetic storm: 2. Comparisons of model predictions with observations, *J. Geophys. Res.*, *92*, 6069–6081, doi:10.1029/JA092iA06p06069.
Förster, M., and N. Jakowski (2000), Geomagnetic storm effects on the topside ionosphere and plasmasphere: A compact tutorial and new results, *Surv. Geophys.*, *21*(1), 47–87, doi:10.1023/A:1006775125220.
Friis-Christensen, E., H. Lühr, D. Knudsen, and R. Haagmans (2008), Swarm—An Earth Observation Mission investigating Geospace, *Adv. Space Res.*, *41*(1), 210–216, doi:10.1016/j.asr.2006.10.008.
Fukao, S., Y. Ozawa, M. Yamamoto, and R. T. Tsunoda (2003), Altitude-extended equatorial spread *F* observed near sunrise terminator over Indonesia, *Geophys. Res. Lett.*, *30*(22), 2137, doi:10.1029/2003GL018383.
Fuller-Rowell, T. J., M. V. Codrescu, R. J. Moffett, and S. Quegan (1994), Response of the thermosphere and ionosphere to geomagnetic storms, *J. Geophys. Res.*, *99*, 3893–3914, doi:10.1029/93JA02015.
Hanson, W. B., B. L. Cargin, and A. Dennis (1986), The effect of vertical drift on the equatorial *F*-Region stability, *J. Atmos. Terr. Phys.*, *48*, 205–212, doi:10.1016/0021-9169(86)90095-4.
Hocke, K., and K. Schlegel (1996), A review of atmospheric gravity waves and traveling ionospheric disturbances: 1982–1995, *Ann. Geophys.*, *12*, 917–940.
Huang, C. M., A. D. Richmond, and M. Q. Chen (2005), Theoretical effects of geomagnetic activity on low-latitude ionospheric electric fields, *J. Geophys. Res.*, *110*, A05312, doi:10.1029/2004JA010994.
Huang, C.-S. (2011), Occurrence of equatorial plasma bubbles during intense magnetic storms, *Int. J. Geophys.*, *2011*, 401,858, doi:10.1155/2011/401858.
Huang, C.-S., S. Sazykin, J. L. Chau, N. Maruyama, and M. C. Kelley (2007), Penetration electric fields: Efficiency and characteristic time scale, *J. Atmos. Terr. Phys.*, *69*(10–11), 1135–1146, doi:10.1016/j.jastp.2006.08.016.
Huang, C.-S., O. de La Beaujardière, P. A. Roddy, D. E. Hunton, J. O. Ballenthin, and M. R. Hairston (2013), Long-lasting daytime equatorial plasma bubbles observed by the C/NOFS satellite, *J. Geophys. Res. Space Physics*, *118*, 2398–2408, doi:10.1002/jgra.50252.
Huang, C.-S., G. R. Wilson, M. R. Hairstone, Y. Zhang, W. Wang, and J. Liu (2016), Equatorial ionospheric plasma drifts and O^+ concentration enhancements associated with disturbance dynamo during the 2015 St. Patrick's Day magnetic storm, *J. Geophys. Res. Space Physics*, *121*, doi:10.1029/2016JA023072.
Kamide, Y., and K. Kusano (2015), No major solar flares but the largest geomagnetic storm in the present solar cycle, *Space Weather*, *13*, 365–367, doi:10.1002/2015SW001213.
Kauristie, K., T. I. Pulkkinen, R. J. Pellinen, and H. J. Opgenoorth (1996), What can we tell about global auroral-electrojet activity from a single meridional magnetometer data?, *Ann. Geophys.*, *14*, 1177–1185, doi:10.1007/s005850050380.
Kelley, M. C., J. J. Makela, O. de Beaujardiére, and J. Retterer (2011), Convective ionospheric storms: A review, *Rev. Geophys.*, *49*, RG2003, doi:10.1029/2010RG000340.
Kikuchi, T., H. Lühr, T. Kitamura, O. Saka, and K. Schlegel (1996), Direct penetration of the polar electric field to the equator during a DP 2 event as detected by the auroral and equatorial magnetometer chains and the EISCAT radar, *J. Geophys. Res.*, *101*, 17,161–17,173, doi:10.1029/96JA01299.
Kobea, A. T., A. D. Richmond, B. A. Emery, C. Peymirat, H. Lühr, T. Moretto, M. Hairston, and C. Amory-Mazaudier (2000), Electrodynamic coupling of high and low latitudes: Observations of May 27, 1993, *J. Geophys. Res.*, *105*, 22,979, doi:10.1029/2000JA000058.
Liou, K., P. T. Newell, B. J. Anderson, L. Zanetti, and C.-I. Meng (2005), Neutral composition effects on ionospheric storms at middle and low latitudes, *J. Geophys. Res.*, *110*, A05309, doi:10.1029/2004JA010840.
Manoj, C., S. Maus, H. Lühr, and P. Alken (2008), Penetration characteristics of the interplanetary electric field to the daytime equatorial ionosphere, *J. Geophys. Res.*, *113*, A12310, doi:10.1029/2008JA013381.
Martinis, C., J. Baumgardner, M. Mendillo, J. Wroten, A. Coster, and L. Paxton (2015), The night when the auroral and equatorial ionospheres converged, *J. Geophys. Res. Space Physics*, *120*, 8085–8095, doi:10.1002/2015JA021555.
Mendillo, M. (2006), Storms in the ionosphere: Patterns and processes for total electron content, *Rev. Geophys.*, *44*, RG4001, doi:10.1029/2005RG000193.
Newell, P. T., T. Sotirelis, K. Liou, C.-I. Meng, and F. J. Rich (2007), A nearly universal solar wind-magnetosphere coupling function inferred from 10 magnetospheric state variables, *J. Geophys. Res.*, *112*, A01206, doi:10.1029/2006JA012015.
Nishida, A. (1968), Coherence of geomagnetic DP 2 fluctuations with interplanetary magnetic variations, *J. Geophys. Res.*, *73*, 5549–5559, doi:10.1029/JA073i017p05549.
Peymirat, C., A. D. Richmond, and A. T. Kobea (2000), Electrodynamic coupling of high and low latitudes: Simulations of shielding/overshielding effects, *J. Geophys. Res.*, *105*, 22,991–23,003, doi:10.1029/2000JA000057.
Pfaff, R., C. Liebrecht, J.-J. Berthelier, M. Malingre, M. Parrot, and J.-P. Lebreton (2008), DEMETER satellite observations of plasma irregularities in the topside ionosphere at low, middle, and sub-auroral latitudes and their dependence on magnetic storms, in Midlatitude Ionospheric Dynamics and Disturbances, edited by Kintner et al., *AGU Monograph*, *181*, 297–310, doi:10.1029/181GM26.
Prölss, G. W. (1993), On explaining the local time variation of ionospheric storm effects, *Ann. Geophys.*, *11*, 1–9.
Prölss, G. W. (1995), Ionospheric *F*-region storms, in *Handbook of Atmospheric Electrodynamics*, vol. 2, edited by H. Volland, pp. 195–248, CRC Press, Boca Raton, Fla.
Prölss, G. W. (2008), Ionospheric storms at mid-latitudes: A short review, in *Midlatitude Ionosheric Dynamics and Disturbances*, *AGU Monograph 181*, edited by P. M. Kintner et al., pp. 9–24, AGU, Washington D. C.
Ramsingh, S., S. Sripathi, S. Sreekumar, K. Banola, P. T. Emperumal, and S. Kumar (2015), Low latitude ionosphere response to super geomagnetic storm of 17/18 March 2015: Results from a chain of ground based observations over Indian sector, *J. Geophys. Res. Space Physics*, *120*, 10,864–10,882, doi:10.1002/2015JA021509.
Rees, D. (1995), Observations and modeling of ionospheric and thermospheric disturbances during major geomagnetic storms: A review, *J. Atmos. Terr. Phys.*, *57*, 1433, doi:10.1016/0021-9169(94)00142-B.
Richmond, A. D., and S. Matsushita (1975), Thermospheric response to a magnetic substorm, *J. Geophys. Res.*, *80*, 2839–2850, doi:10.1029/JA080i019p02839.
Richmond, A. D., C. Lathuillere, and S. Vennerstroem (2003), Winds in the high-latitude lower thermosphere: Dependence on the interplanetary magnetic field, *J. Geophys. Res.*, *108*(A2), 1066, doi:10.1029/2002JA009493.
Rishbeth, H. (1991), *F* -region storms and thermospheric dynamics, *J. Geomagn. Geoelectr.*, *43*(suppl.), 513, doi:10.5636/jgg.43.Supplement1_513.
Rishbeth, H., and O. K. Garriott (1969), *Introduction to Ionospheric Physics*, *Int. Geophys. Ser.*, vol. 14, Elsevier, New York.

Ritter, P., H. Lühr, and E. Doornbos (2010), Substorm-related thermospheric density and wind disturbances derived from CHAMP observations, *Ann. Geophys.*, *28*, 1207–1220, doi:10.5194/angeo-28-1207-2010.

Rodger, A. S., G. L. Wrenn, and H. Rishbeth (1989), Geomagnetic storms in the Antarctic *F* region, II, physical interpretation, *J. Atmos. Terr. Phys.*, *51*, 851–866, doi:10.1016/0021-9169(89)90002-0.

Stolle, C., C. Manoj, H. Lühr, S. Maus, and P. Alken (2008a), Estimating the daytime equatorial ionization anomaly strength from electric field proxies, *J. Geophys. Res.*, *113*, A09310, doi:10.1029/2007JA012781.

Stolle, C., H. Lühr, and B. G. Fejer (2008b), Relation between the occurrence rate of ESF and the equatorial vertical plasma drift velocity at sunset derived from global observations, *Ann. Geophys.*, *26*, 3979–3988, doi:10.5194/angeo-26-3979-2008.

Su, S.-Y., C. K. Chao, and C. H. Liu (2008), On monthly/seasonal/longitudinal variations of equatorial irregularities occurrences and their relationship with the post-sunset vertical drift velocity, *J. Geophys. Res.*, *113*, A05307, doi:10.1029/2007JA012809.

Sultan, P. J. (1996), Linear theory and modeling of the Rayleigh-Taylor instability leading to the occurrence of equatorial spread *F*, *J. Geophys. Res.*, *101*, 26,875–26,891, doi:10.1029/96JA00682.

Tapley, B. D., S. Bettadpur, M. Watkins, and C. Reigber (2004), The gravity recovery and climate experiment: Mission overview and early results, *Geophys. Res. Lett.*, *31*, L09607, doi:10.1029/2004GL019920.

Tulasi Ram, S., et al. (2016), Dusk side enhancement of equatorial zonal electric field response to convection electric fields during the St. Patrick's Day storm on March 17, 2015, *J. Geophys. Res. Space Physics*, *121*, 538–548, doi:10.1002/2015JA021932.

Xiong, C., J. Park, H. Lühr, C. Stolle, and S. Y. Ma (2010), Comparing plasma bubble occurrence rates at CHAMP and GRACE altitudes during high and low solar activity, *Ann. Geophys.*, *28*, 1647–1658, doi:10.5194/angeo-28-1647-2010.

Xiong, C., H. Lühr, S. Y. Ma, C. Stolle, and B. G. Fejer (2012), Features of highly structured equatorial plasma irregularities deduced from CHAMP observations, *Ann. Geophys.*, *30*, 1259–1269, doi:10.5194/angeo-30-1259-2012.

Xiong, C., H. Lühr, H. Wang, and M. G. Johnsen (2014), Determining the boundaries of the auroral oval from CHAMP field-aligned current signatures—Part 1, *Ann. Geophys.*, *32*, 609–622, doi:10.5194/angeo-32-609-2014.

Xiong, C., H. Lühr, S. Y. Ma, and K. Schlegel (2015), Validation of GRACE electron densities by incoherent scatter radar data and estimation of plasma scale height in the topside ionosphere, *Adv. Space Res.*, *55*(8), 2048–2057, doi:10.1016/j.asr.2014.07.022.

Xiong, C., H. Lühr, and B. G. Fejer (2016), The response of equatorial electrojet, vertical plasma drift and thermospheric zonal wind to enhanced solar wind input, *J. Geophys. Res. Space Physics*, *121*, 5653–5663, doi:10.1002/2015JA022133.

Yamazaki, Y., and M. J. Kosch (2015), The equatorial electrojet during geomagnetic storms and substorms, *J. Geophys. Res. Space Physics* , *120*, 2276–2287, doi:10.1002/2014JA020773.